materials

MDPI

Article

Europium(III)-Doped Gadolinium(III) Complex for High-Sensitivity Temperature Sensing in the Physiological Range

Kevin Soler-Carracedo [1,*], María Díaz-González [1], Inocencio R. Martin [1,2], Susana Rios [1], Beatriz Gil-Hernández [2,3], Gabriela Brito-Santos [3] and Joaquín Sanchiz [2,3]

[1] Departamento de Física, Universidad de La Laguna, Apdo. 456, E-38200 San Cristóbal de La Laguna, Spain
[2] Instituto Universitario de Materiales y Nanotecnología (IMN), Universidad de La Laguna, Apdo. 456, E-38200 San Cristóbal de La Laguna, Spain
[3] Departamento de Química, Facultad de Ciencias, Universidad de La Laguna, Apdo. 456, E-38200 San Cristóbal de La Laguna, Spain
* Correspondence: ksolerca@ull.edu.es

Abstract: A new Eu^{3+}-doped Gd^{3+} complex of formula $[Eu_{0.0135}Gd_{0.9865}(pta)_3me\text{-}phen]$ was synthesized and structurally characterized (Hpta = benzoyltrifluoroacetone, me-phen = 5-methyl-1,10-phenanthroline). The photoluminescence study revealed that when the compound was excited at RT, under a 457 nm continuous laser, the material exhibited high luminescence due to the antenna effect of the ligands, as well as a good balance between the phosphorescence from the spin-forbidden triplet (from the organic ligands), and the characteristic lanthanide f-f transitions. The ratio between the previous emissions drastically changed when the sample was heated up to 62 °C inside a tubular furnace. This ratio was investigated using the luminescence intensity ratio method, to analyze the capabilities of the sample as a temperature sensor. The relative sensitivity reached a maximum of 11.4 $°C^{-1}$ %, maintaining a detection limit below 0.15 °C for the whole temperature range.

Keywords: hybrid organic-inorganic complex; optical temperature sensor; luminescence; downshifting

Citation: Soler-Carracedo, K.; Díaz-González, M.; Martin, I.R.; Rios, S.; Gil-Hernández, B.; Brito-Santos, G.; Sanchiz, J. Europium(III)-Doped Gadolinium(III) Complex for High-Sensitivity Temperature Sensing in the Physiological Range. *Materials* **2022**, *15*, 7501. https://doi.org/10.3390/ma15217501

Academic Editors: Fabian Ambriz Vargas and Jianzhong Zhang

Received: 12 September 2022
Accepted: 21 October 2022
Published: 26 October 2022

1. Introduction

In recent years, much effort has been devoted to developing lanthanide ratiometric thermometers based on the temperature-induced changes in the luminescence intensity of two different transitions [1,2]. Lanthanide ions are fundamental in all luminescence science research and are usually employed in optical sensors due to their interesting optical properties. In particular, numerous research works have investigated trivalent lanthanide ions, so their optical properties are relatively well known [3]. These ions feature 4f-electrons' shielding, which is related to their characteristic sharp absorption and emission spectra covering a wide UV–Vis–NIR range.

The host material plays an essential role in the design of optical devices, as its vibratory properties can influence the optical behavior of the dopant ion. Many of the transition lines (of practical importance) of lanthanide ions originate from excited levels with a small energy gap. Therefore, material hosts with lower phonon energy are necessary, in order for the radiative transitions of active ions to dominate over non-radiative losses. Furthermore, lanthanide ions present weak light absorption, which translates into weak luminescence, since the luminescence intensity is proportional to the absorption [4,5]. Hybrid organic–inorganic compounds can overcome this problem by providing an intense absorption band from an organic ligand that will transfer the higher absorbed-light energy to the lanthanide ion. This effect is known as the antenna effect (or sensitization) [6]. On top of that, they are easy to process (and, therefore, to mix), to create composites that can combine temperature sensing with other novel and interesting applications [7–9].

In this work, we study the capability of the Ln(III) complex [$Eu_{0.0135}Gd_{0.9865}(pta)_3$me-phen] as an optical temperature ratiometric sensor. Ratiometric thermometers based on dual-emission provide a self-calibrated temperature readout that is unaffected by sensor concentration and/or excitation-signal fluctuations. Thus, these thermometers are more reliable and accurate than thermometers based on the emission intensity of a single transition [10–12]. This type of dual-emission measurement is commonly comprehended as being part of the luminescence intensity ratio (LIR) or fluorescence intensity ratio (FIR) techniques, and is based mainly in the exploit of pairs of thermalized energy levels in trivalent lanthanide-doped materials that can be fitted to a Boltzmann equation. This classic approach, has limited sensitivity in the sensors, proportional to the energy gap between the thermalized levels [13]. By using a complex material, combining organic and inorganic emissions, however, it is possible to overcome the previous sensitivity limit of the Boltzmann thermometer. This work may be considered as part of an exciting new trend, related to overcoming the previously-mentioned limit. Other approaches include the combination of linear and non-linear optics, whether by second-harmonic generation [14–16] or multilevel cascade [17], as well as the combination of a single-emission band and the conventional Boltzmann ratio [18].

2. Experimental Setup

2.1. Synthesis

Reagents: all chemicals and reagents were commercially available and used without further purification; specifically, benzoyltrifluoroacetone 99% (Hpta), 5-methyl-1,10-phenanthroline (me-phen) 99%, triethylamine 99%, ethanol, and $Eu(NO_3)_3{\cdot}5H_2O$ (99.9%), $Gd(NO_3)_3{\cdot}6H_2O$ (99.9%). All the reactions were performed under a dinitrogen atmosphere.

Synthesis of [$Eu_{0.0135}Gd_{0.9865}(pta)_3$me-phen]: Hpta (163.8 mg, 0.75 mmol) and triethylamine (150 µL, 1.00 mmol) were dissolved in 9 mL of ethanol in a round-bottomed flask. Then, 0.25 mmol of me-phen (48.6 mg) dissolved in 3 mL of ethanol was added. Subsequently, 0.0034 mmol of $Eu(NO_3)_3{\cdot}5H_2O$ (1.5 mg) and 0.2466 mmol of $Gd(NO_3)_3{\cdot}6H_2O$ (111.3 mg), for a sum of 0.25 mmol of $Ln(NO_3)_3$, were dissolved together in 3 mL of ethanol and added to the reaction flask. The solution was heated under stirring at 60 °C for 150 min. After that, the solution was cooled to room temperature and 10 mL of deionized water was added. A white precipitate appeared immediately, and the solution was stirred for another 15 min. The product was collected by filtration, washed with 10 mL of water and 5 mL of ice-cooled ethanol, and dried at 60 °C overnight. The crude product was recrystallized by diffusion of n-heptane in an acetonitrile solution of the complex. During the recrystallization process, some crystals were collected for single-crystal X-ray diffraction, to solve the structure, and the rest was ground, for: X-ray powder diffraction, elemental analysis, thermogravimetry and photoluminescence measurements. Synthesised [$Eu_{0.0135}Gd_{0.9865}(pta)_3$me-phen] yield: 210.1 mg (85%). Elemental analysis (%) calculated for $C_{43}H_{28}N_2Eu_{0.0135}Gd_{0.9865}O_6F_9$ (996.85): C, 51.75; H, 2.80; N, 2.81. Found: C, 51.8; H, 2.8; N, 2.9. IR (KBr, ν/cm^{-1}): 3070(m), 2921(m), 1612(s), 1577(s), 1527(m), 1319(s), 1292(s), 1187(s), 1139(s), 1078(w), 767(m), 703(m), 603(m), 582(m). UV-vis (ethanol, λ_{max}/nm): 232, 266, 324.

2.2. General Characterization Methods

FT-IR as KBr disks, in the 400 cm^{-1} to 4000 cm^{-1} range, was recorded on a Thermo NicolletAvatar 360 FT-IR spectrometer (Nicolet Instruments, Madison, WI, USA). UV-visible spectra, between 220 nm and 800 nm, with samples dissolved in ethanol, were recorded on a Varian Cary 50 bio UV-Visible spectrophotometer (Agilent Technologies, Santa Clara, CA, USA). X-ray powder diffraction patterns were recorded on a PANanalytical X'pert X-ray diffractometer (Malvern Panalytical, Malvern, United Kingdom) with Cu Kα radiation, 1.54184 Å, at room temperature.

2.3. Single-Crystal X-ray Crystallography

A suitable single crystal was selected under a polarizing microscope, taken directly from the mother liquors, and covered with a protective oil before putting it on a 0.05 mm loop. Single-crystal XRD data were collected with an Agilent SuperNova diffractometer (Agilent Technologies, Santa Clara, CA, USA), with a micro-focus X-ray, under Cu-K_α radiation (λ = 1.5418 Å). CrysalisPro software (v1.171.41.122a ,Rigaku Corporation, Tokyo, Japan, 2021) was used to collect, index, scale and apply analytical absorption correction, based on the multi-scan method.

2.4. Structure Analysis and Refinement

The structure was solved by direct methods, using SHELXT2018/2 [19], and refinement was undertaken via full-matrix least-squares on F^2, using SHELXL2018/3 [19]. Crystal data and details of the structure refinement are given in Table 1. Crystallographic data for the structure have been deposited in the Cambridge Crystallographic Database with deposition number 2162029. The structure was solved considering all the Ln atoms as Gd, since it corresponds to 98.65 % of the total Ln. The formula and the distances and angles in Tables 1 and 2 refer to this element.

Table 1. Crystal data and structure refinement details.

Compound	**[Gd(pta)$_3$me-phen]** [a]
CCDC Number	2162029
Empirical formula	$C_{43}H_{27}F_9GdN_2O_6$
M/gmol^{-1}	995.91
Temperature (K)	293
λ/Å	1.54184
Crystal system	Monoclinic
space group	$P2_1/c$
a, (Å)	10.0369 (3)
b, (Å)	37.5293 (15)
c, (Å)	11.1039 (3)
β (°)	91.093 (3)
V (Å^3)	4181.8 (2)
Z	4
D_{calc}/gcm^{-3}	1.582
μ/(mm^{-1})	11.05
Theta range/°	4.6–72.3
R_{int}	0.038
$R_1[I > 2\sigma(I)]$ [b]	0.0895
wR_2[I > 2σ(I)] [c]	0.1575
GOF onF^2 [d]	1.053

[a] The compound is formulated this way for simplicity. [b] $R_1 = [\sum(\|F_o| - |F_c|\|)/\sum|F_o|]$. [c] $wR_2 = [\sum[w(F_o^2 - F_c^2)^2]/\sum[w(F_o^2)^2]]^{1/2}$. [d] Goodness-of-fit $S = [\Sigma\,[w(F_o^2 - F_c^2)^2]/(n-p)]^{1/2}$.

Aromatic hydrogen atoms and hydrogen atoms in the alpha-position of benzoyltrifluoroacetone ligand's diketonate group were situated geometrically (C-H = 0.95 Å) and refined using a riding model (AFIX 43) with U_{iso}(H) = 1.2 U_{eq}(C). The Methyl group's hydrogens in the phenanthroline ring were also positioned geometrically (C-H = 0.98 angstroms) and refined using a riding model (AFIX 137) with U_{iso}(H) = 1.5 U_{eq} (C). This methyl group is disordered over positions 5 and 6 of the phenanthroline ring and was refined with PART instructions, with occupancies of 0.42:0.58. The phenyl ring of the benzoyltrifluoroacetone ligand labelled A was refined using a riding model AFIX 66.

2.5. X-ray Powder Diffractograms

There was a perfect match between the simulated (from single-crystal structure) diffractogram and the experimental powder diffractogram (Figure 1), which confirmed the integrity of the product sample and allowed us to use the recrystallized material for the rest

of the measurements. Figure 1 also shows the isostructural character of [Gd(pta)$_3$me-phen] and [Eu(pta)$_3$me-phen] [20].

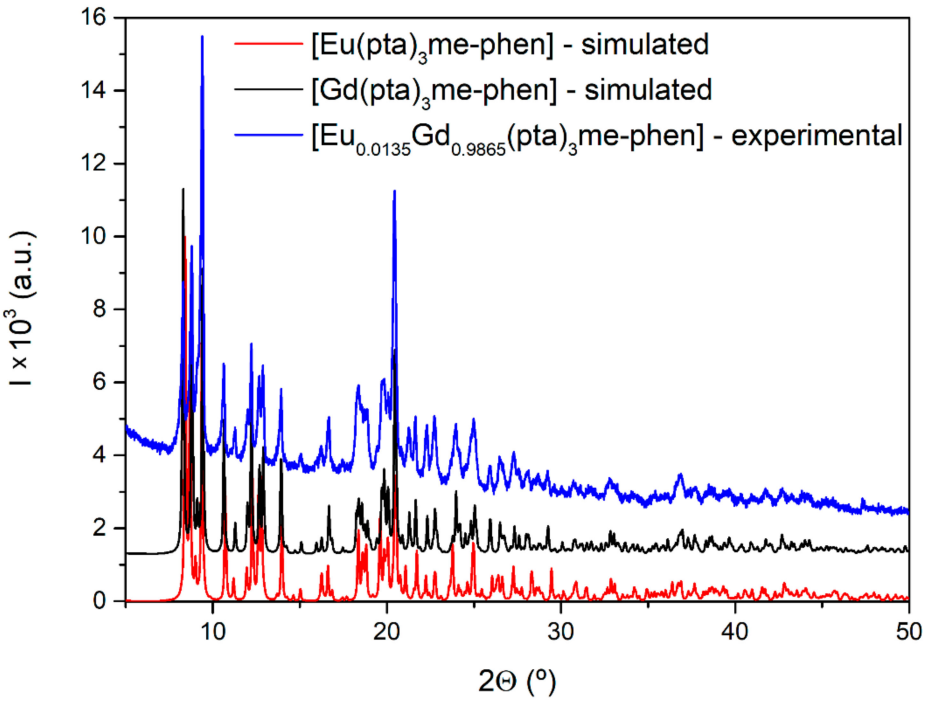

Figure 1. Simulated and experimental powder diffractograms.

2.6. Optical Characterization

The emission spectra for the sample were obtained by excitation with a 457 nm continuous laser, with the emission focused onto an optical fiber, coupled to a 0.303 m grating single spectrometer (Andor Shamrock SR-303i-A from Andor Technology Ltd, Belfast, United Kingdom). For the detection, a cooled Newton CCD camera (Andor Technology Ltd, Belfast, United Kingdom) was used. All spectra were corrected from the respective spectral response of the equipment.

For the temperature calibration, the same setup was used, with the sample placed inside a closed tubular furnace (Gero RES-E 230/3 from Carbolite Gero, Derbyshire, UK), controlled via contact with a type K thermocouple (Figure 2):

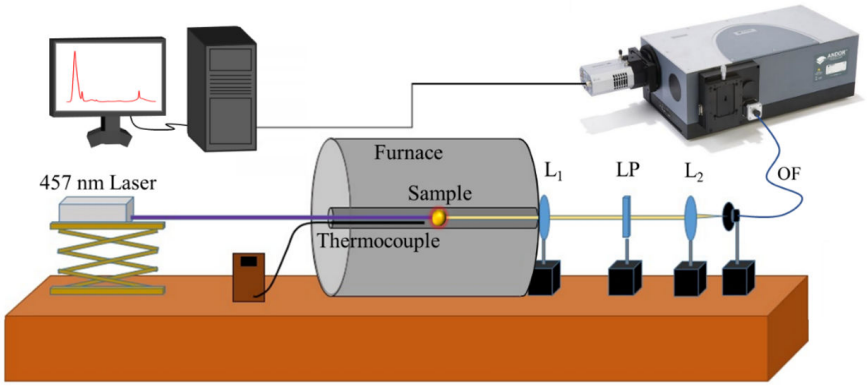

Figure 2. Experimental setup used for the temperature calibration of the emission spectra.

where L1 and L2 are lenses, LP is a Long Pass filter and OF corresponds to the optical fiber that collects the signal.

3. Results and Discussion

3.1. Structure of the Compound

$[Eu_{0.0135}Gd_{0.9865}(pta)_3me\text{-}phen]$ crystallizes in the monoclinic $P2_1/c$ space-group and has a molecular structure. The Gd^{3+} and the Eu^{3+} ions are randomly dispersed throughout the material and occupy the same crystallographic positions, replacing each other. The Ln^{3+} ions are bound to three β-diketonate (A, B and C) and to one 5-methyl-phenanthroline ligand, (Figure 3). The me-phen ligand shows its typical coordination mode, with the two donor nitrogen atoms directly bound to the Ln^{3+} ion. The pta^- ligands bind the Ln^{3+} ion through the two oxygen atoms, forming five-membered chelate rings. The Ln^{3+} atoms are in an eight-coordination structure, with a distorted square–antiprismatic geometry, surrounded by six oxygen atoms from the three diketonate ligands, with distances in the range 2.3361(1) Å to 2.3574(1) Å and, furthermore, surrounded by the two nitrogen atoms of the 5-methyl-phenanthroline, at distances 2.5491(1) Å-2.5880(1) Å, (Figure 3b). The distances and angles are in the expected range, in agreement with similar complexes (Table 2) [21,22].

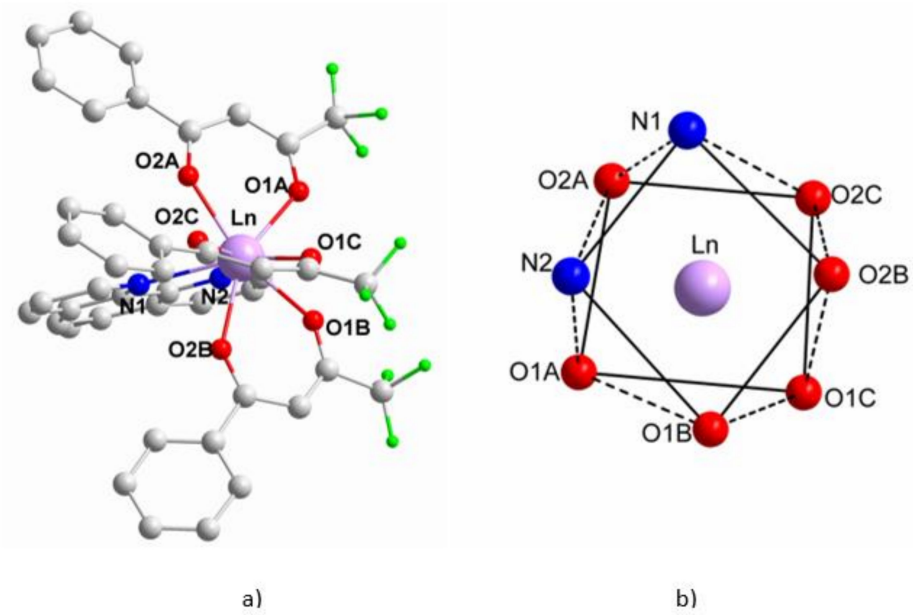

Figure 3. (**a**) molecular structure of $[Eu_{0.0135}Gd_{0.9865}(pta)_3me\text{-}phen]$, hydrogen atoms omitted for clarity; (**b**) square–antiprismatic environment around the Ln^{3+} ion.

Table 2. Selected bond distances (Å) and angles (°).

Gd1—O2A	2.3361(1)	Gd1—O2C	2.3370(1)
Gd1—O1A	2.3444(1)	Gd1—N2	2.5491(1)
Gd1—O1C	2.3470(1)	Gd1—N1	2.5880(1)
Gd1—O2B	2.3574(1)		
O2A—Gd1—N2	85.648(1)	O1C—Gd1—O2C	71.629(1)
O1A—Gd1—O2A	71.780(1)	O2B—Gd1—O2C	76.567(1)
O1A—Gd1—O1C	85.241(1)	N1—Gd1—O2B	70.877(1)
N1—Gd1—N2	62.421(1)		

Table 3 shows the intramolecular hydrogen bonding distances. Those between one of the diketonate oxygen atoms and the closest phenylene hydrogen range from 2.4159(1) Å to 2.4937(1) Å. Additionally, in those between the diketonate hydrogen and one of the F atoms, the range is 2.3378(1) Å – 2.2769(1) Å. These hydrogen bonds block the twist of the phenylene ring with respect to the diketonate group (twisting angles in the range of

13.58° to 24.36°), enhancing the conjugation and the rigidity of the molecule favoring the luminescence process [23–25].

Table 3. Intramolecular hydrogen bonding distances in Å.

F3A-H16A	2.3378(1)	O2A—H19A	2.4159(1)
F3C-H16C	2.3769(1)	O2B—H23B	2.4937(1)
F1B-H16B	2.3629(1)	O2C—H19C	2.4520(1)

The packing diagram, Figure 4, shows the molecular structure of the complex. Weak intermolecular interactions favor the complex's solubility in solvents such as CH_2Cl_2 or CH_3CN. The voluminous character of the ligands and the high coordination number of the complex prevents the entry of water molecules into the coordination sphere of the metal ion, which would deactivate the molecule by non-radiative vibrating processes [25].

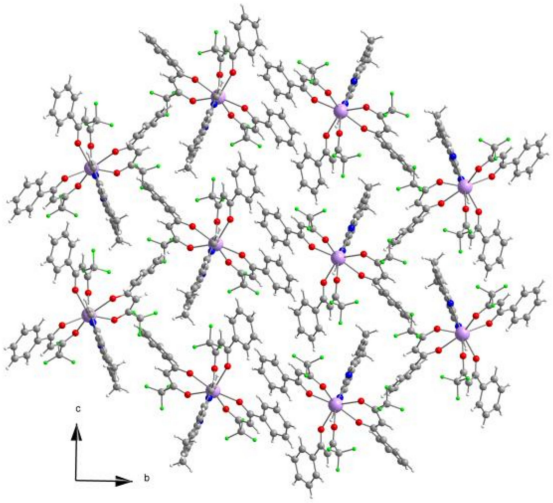

Figure 4. Packing diagram of the structure of $[Eu_{0.0135}Gd_{0.9865}(pta)_3me\text{-}phen]$.

3.2. Emission Spectrum and Temperature Sensor

The emission spectrum of the Eu^{3+}-doped Gd^{3+} complex under 457 nm continuous laser excitation is shown in Figure 5a. Two different emissions can be seen superimposed in the spectrum. First, the characteristic emission bands of Eu^{3+} at 595 nm ($^5D_0 \rightarrow {}^7F_1$), 611 nm ($^5D_0 \rightarrow {}^7F_2$), 647 nm ($^5D_0 \rightarrow {}^7F_3$), and 696 nm ($^5D_0 \rightarrow {}^7F_4$); second, a broad emission band centered at 550 nm and related to the $T_1 \rightarrow S_0$ phosphorescence from the organic ligands [26].

According to the spectrum shown in Figure 5a, Figure 5b shows a schematic diagram of the energy levels in the lanthanide ions and the ligands, along with the energy transfers involved in the luminescence process. The 457 nm laser radiation excites the pta^- ligand from the ground singlet state to the excited singlet state. At this point, ISC to the excited triplet states of the pta^- and me-phen takes place, then energy transfer (ET) to the excited states of the Eu^{3+} ion occurs. Finally, the decay to the ground states of the Eu^{3+} ion produces the luminescence. The laser at 457 nm can also directly excite the Eu^{3+} ion to its $^5D_2$ state, and after a non-radiative decay to the $^5D_0$ state, luminescence occurs. These processes compete with the phosphorescence (P) of the ligands. A time decay of 0.44 ms for the Eu^{3+} $^5D_0$ state was obtained, which is in good agreement with the literature and can be related to a good sensitization [27,28]. Changes in the temperature produce differences in the relationship between both decay pathways, and this forms the base of temperature sensing. Given the absence of UV-excitation sources, no contribution to the luminescence is expected from the Gd^{3+} ions.

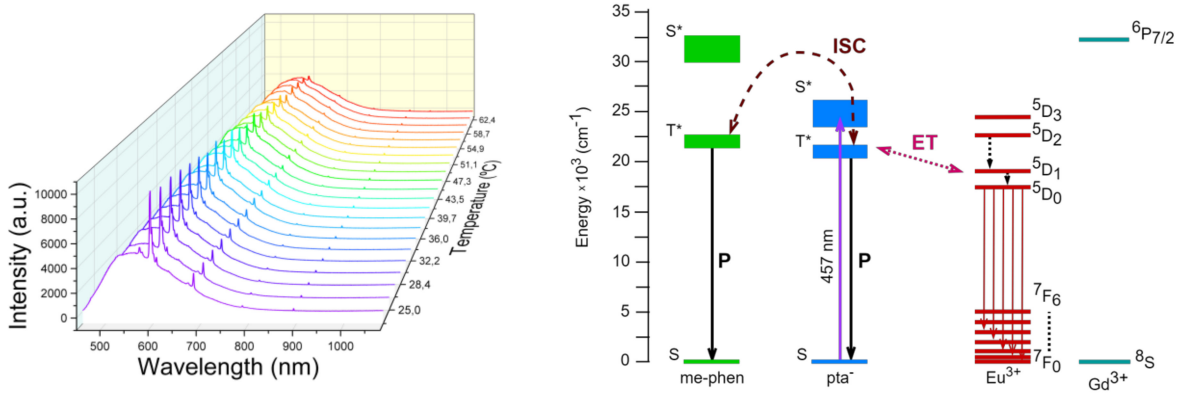

(**a**) (**b**)

Figure 5. (**a**) Emission spectra of $[Eu_{0.0135}Gd_{0.9865}(pta)_3me\text{-}phen]$ under 457 nm in the range of 23–62 °C; (**b**) Partial energy-level diagram indicating the transitions observed under the excitation of the 457 nm laser where ISC (intersystem crossing) occurs; ET is energy transfer; P is phosphorescence. Non-radiative relaxation processes are represented by dashed arrows [29].

The sample's response calibration with temperature was performed by introducing the sample into a furnace and heating the system from RT up to 62 °C (Figure 5a). A thermal redistribution of the population was observed and the ratio of intensities between the emission bands of Eu^{3+} and the organic ligands drastically changed, reaching a change of over one order of magnitude for a 40 °C range increase. Following this behavior, the LIR was used to calibrate the temperature between the emission related to the organic compound and the Eu^{3+} $^5D_0 \rightarrow {}^7F_2$ (611 nm) emission band (Figure 6). Given the not-well-resolved state of the emissions, the ratio was obtained by means of the separation of chosen wavelength regions. This method was chosen for its simplicity, although it is worth mentioning that spectral deconvolution could lead to a slight increase in terms of relative sensitivity [13]. Integration from 470 to 580 nm was collected for the organic emission, whereas for the Eu3+ transition the integration was collected from 605 to 625, after applying a baseline subtraction. The obtained data were fitted to a Boltzmann-type equation.

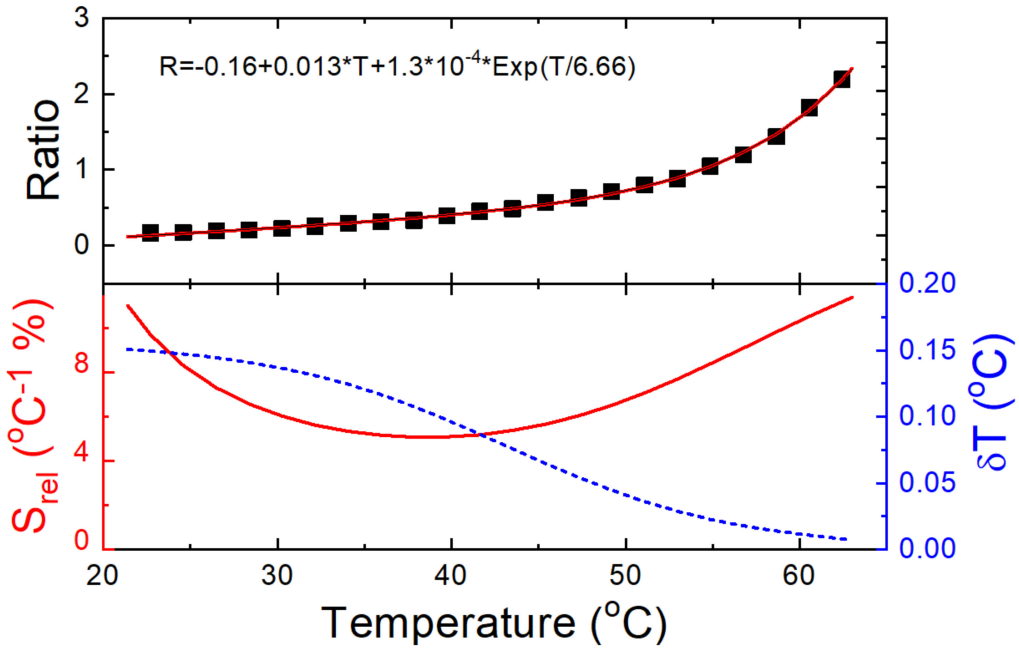

Figure 6. Ratio measurements as a function of temperature (top), relative sensitivity (bottom—continuous red line) and temperature uncertainty (bottom—dashed blue line).

To characterize the performance of the sample as a temperature sensor, the relative sensitivity and the temperature uncertainty were obtained and presented in Figure 6. The relative sensitivity is a magnitude defined by the rate at which the measured parameter (Δ) changes with respect to temperature and is given by

$$S_{rel} = \frac{1}{\Delta}\left|\frac{d\Delta}{dT}\right| \cdot 100 \quad (1)$$

In this experiment the measured parameter (Δ) was calculated as the ratio between the emission related to the organic compound and the Eu^{3+} $^5D_0 \rightarrow {}^7F_2$ (611 nm) emission band (LIR).

In contrast to the absolute sensitivity, the relative sensitivity magnitude allows for the comparison of sensors independently, on the physical parameter analyzed as a function of temperature. Figure 6 shows maximums of 11 $°C^{-1}$ % and 11.4 $°C^{-1}$ % for temperatures of 23 °C and 62 °C, respectively, with a minimum of 5.1 $°C^{-1}$ % at 40 °C. Higher values for the relative sensitivity could be achieved over 62 °C, but they were considered outside the reliability criterion of the intensity of the sensor when above 5% of the noise level [30]. In Table 4, a list of optical temperature sensors based on Eu^{3+}-doped lanthanide ions is ranked by relative sensitivity. Outside of this study (as far as can be ascertained), no sensor within this reliability criterion has achieved this high level of relative sensitivity in the physiological range. A sensor by X. Lui et al. [31], with relative sensitivity of 31 $\%K^{-1}$ at 4 K, presented values below 1 $\%K^{-1}$ in the physiological range. The sensor by X. Yang et al. [32], with a relative sensitivity of 16 $\%K^{-1}$ at 383 K, also showed a maximum of 9.01 $\%K^{-1}$ over the physiological range, while the sensor by A. Kovalenko et al. [33] was analyzed for a range of temperatures well below this range.

Table 4. List of optical temperature sensors based on Eu^{3+}-doped lanthanide ions, ranked by relative sensitivity.

Host	Doped Ions	Temp Range (K)	T_{max} (K)	Max S_r (% K^{-1})	Refs
H_4L	Tb^{3+}/Eu^{3+}	4–290	4	31	[31]
BTC	Tb^{3+}/Eu^{3+}	298–383	383	16	[32]
$(L^1)(HL^1)$	Eu^{3+}	80–180	125	12	[33]
$(pta)_3$me-phen	Eu^{3+}/Gd^{3+}	296–335	335	11.4	This work
$CaMoO_4$	Tb^{3+}/Eu^{3+}	298–603	603	9.50	[34]
HOF-TCBP	Eu^{3+}	297–377	297	5.79	[35]
$L(DMF)_2(NO_3)$	Tb^{3+}/Eu^{3+}	10–300	250	4.90	[36]
UiO-66	Zr^{3+}/Eu^{3+}	237–337	337	4.67	[37]
Ln@Al(OH)(bpydc)	Tb^{3+}/Eu^{3+}	283–333	333	3.00	[38]
ZJU88 ⊃ ⋂perylene	Eu^{3+}	293–353	293	1.28	[11]
β-$NaY_{0.8}Gd_{0.2}F_4$	Tb^{3+}/Eu^{3+}	303–563	303	0.76	[39]
POM@MOF	Tb^{3+}/Eu^{3+}	60–360	60	0.71	[40]
CGS	Tb^{3+}/Eu^{3+}	313–473	473	0.56	[41]
$Ca_8ZnLa(PO_4)_7$	Tb^{3+}/Eu^{3+}	298–498	298	0.53	[42]
[Ln(hfa)$_3$(dpbp)]n	Tb^{3+}/Eu^{3+}	200–300	200	0.52	[43]
$Gd_2(MoO_4)_3$	Tb^{3+}, Eu^{3+}	80–450	270	0.50	[44]
$NaYF_4$	$Ce^{3+}/Tb^{3+}/Eu^{3+}$	303–573	573	0.46	[45]
CaF_2	Tb^{3+}/Eu^{3+}	21–320	21	0.40	[46]
YF_3	Tb^{3+}/Eu^{3+}	303–563	563	0.38	[47]
Borate glass	Tb^{3+}/Eu^{3+}	353–573	573	0.35	[48]
$[Ln(bdc)_{1.5}(H_2O)_2]$	Tb^{3+}/Eu^{3+}	290–320	318	0.31	[49]
SiO_2–Y_2O_3	Tb^{3+}/Eu^{3+}	298–333	303	0.29	[50]
YF_3	$Ce^{3+}/Tb^{3+}/Eu^{3+}$	303–563	563	0.20	[47]
$Sr_3GdNa(PO_4)_3F$	Tb^{3+}/Eu^{3+}	303–483	303	0.16	[51]
YF_3 glass	Tb^{3+}/Eu^{3+}	303–563	563	0.13	[52]
$[Ln_2(D\text{-cam})(Himdc)_2(H_2O)_2]$	Tb^{3+}/Eu^{3+}	100–450	450	0.11	[53]

Finally, to characterize the error of the sensor, the temperature uncertainty (or temperature resolution) was calculated. Temperature uncertainty refers to the minimum temperature change that can be detected in a given measurement by the sensor and is given by [30]

$$\delta T = \frac{1}{S_{rel}} \frac{\delta \Delta}{\Delta} \quad (2)$$

where $\delta\Delta$ corresponds to the uncertainty in the determination of the Δ. To obtain this last parameter experimentally, 100 measurements were carried out on with the sample at RT, in the same conditions, where the temperature-dependent measurements were undertaken. The resulting LIR readouts and the respective standard deviation are presented in Figure 7. The experimental uncertainty in the determination is considered as the standard deviation for the LIR readouts ($\delta\Delta$ equal to 0.002). Using this parameter in Equation (2), the resulting minimum and maximum temperature uncertainties are 0.008 and 0.15 °C for the temperatures of 62 and 23 °C, respectively (Figure 6). Both results are well below the inner limit of precision that can be found in cell-temperature sensing, among other applications [54].

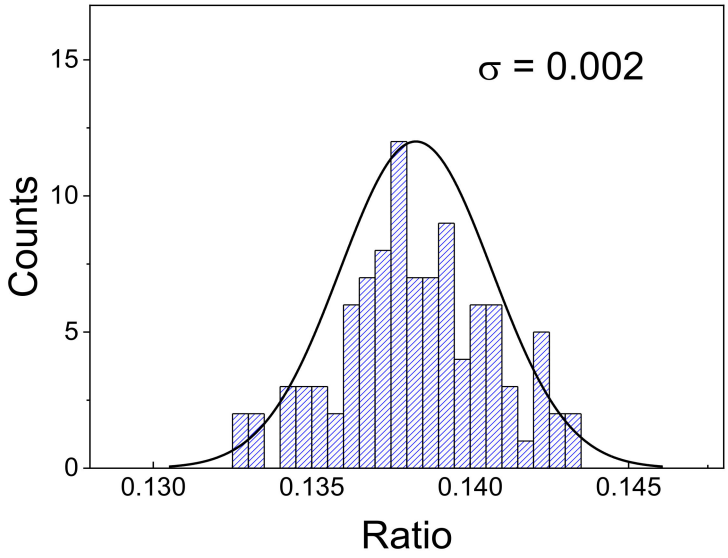

Figure 7. Distribution of the measured parameter (LIR) and the corresponding standard deviation.

4. Conclusions

A coordination compound combining pta$^-$ and me-phen ligands with Eu^{3+} and Gd^{3+} lanthanide ions was successfully synthesized and characterized. When excited under a 457 nm continuous laser, the emission spectrum showed a balanced equilibrium between the broad phosphorescence from the organic ligands and the sharp peaks from the Eu^{3+} at RT. When the sample was heated in the physiological temperature range, up to 62 °C, a drastic change was observed in the intensities between the organic phosphorescence and the lanthanide luminescence. The ratio of these intensities was analyzed by the LIR technique. Furthermore, the performance of the sample as a temperature sensor was studied by obtaining its relative sensitivity and temperature uncertainty. The relative sensitivity presents, as far as can be ascertained, the highest sensitivities recorded to date for organic–inorganic hybrid materials. The temperature uncertainty in the study presented values below 0.15 °C for the whole temperature range. All of these results position $[Eu_{0.0135}Gd_{0.9865}(pta)_3$me-phen] as one of the top candidates for optical temperature sensing in the physiological range.

Author Contributions: K.S.-C.—Writing, original draft; M.D.-G.— Investigation, data curation, visualization; I.R.M.—Methodology, supervision, writing, review & editing; S.R.—Methodology and conceptualization; B.G.-H.—Formal analysis, data curation; G.B.-S.—Investigation, resources; J.S.—Supervision, writing, review & editing. All authors have read and agreed to the published version of the manuscript.

Funding: This work was financially supported by Ministerio de Ciencia e Innovacion of Spain (MICIIN) under the National Program of Sciences and Technological Materials (PID2019-106383GB-C44 and PID2019-107335RA-I00) and Gobierno de Canarias (PROID2021010102 and PROID2020010067) and EU-FEDER funds.

Institutional Review Board Statement: Not applicable.

Informed Consent Statement: Not applicable.

Data Availability Statement: The data presented in this study are available on request from the corresponding author. The data are not publicly available due to own empirical research of corresponding author.

Conflicts of Interest: The authors declare no conflict of interest.

References

1. Dramićanin, M.D. Trends in luminescence thermometry. *J. Appl. Phys.* **2020**, *128*, 040902. [CrossRef]
2. Ananias, D.; Almeida Paz, F.A.; Carlos, L.D.; Rocha, J. Near-Infrared Ratiometric Luminescent Thermometer Based on a New Lanthanide Silicate. *Chem.—A Eur. J.* **2018**, *24*, 11926–11935. [CrossRef] [PubMed]
3. Wade, S.A. Temperature Measurement Using Rare Earth Doped Fibre Fluorescence. Doctoral Dissertation, Victoria University, Footscray, Australia, 1999.
4. Binnemans, K. Lanthanide-Based Luminescent Hybrid Materials. *Chem. Rev.* **2009**, *109*, 4283–4374. [CrossRef] [PubMed]
5. Kitagawa, Y.; Suzue, F.; Nakanishi, T.; Fushimi, K.; Hasegawa, Y. A highly luminescent Eu(iii) complex based on an electronically isolated aromatic ring system with ultralong lifetime. *Dalton Trans.* **2018**, *47*, 7327–7332. [CrossRef] [PubMed]
6. Weissman, S. Intramolecular Energy Transfer The Fluorescence of Complexes of Europium. *J. Chem. Phys.* **1942**, *10*, 214–217. [CrossRef]
7. Zan, G.; Wu, T.; Dong, W.; Zhou, J.; Tu, T.; Xu, R.; Chen, Y.; Wang, Y.; Wu, Q. Two-Level Biomimetic Designs Enable Intelligent Stress Dispersion for Super-Foldable C/NiS Nanofiber Free-Standing Electrode. *Adv. Fiber Mater.* **2022**, *4*, 1177–1190. [CrossRef]
8. Hasan, M.; Hossain, M.; Chowdhury, H.K. Two-dimensional MXene-based flexible nanostructures for functional nanodevices: A review. *J. Mater. Chem. A* **2021**, *9*, 3231–3269. [CrossRef]
9. Zan, G.; Wu, T.; Zhu, F.; He, P.; Cheng, Y.; Chai, S.; Wang, Y.; Huang, X.; Zhang, W.; Wan, Y.; et al. A biomimetic conductive super-foldable material. *Matter* **2021**, *4*, 3232–3247. [CrossRef]
10. Li, L.; Zhu, Y.; Zhou, X.; Brites, C.D.S.; Ananias, D.; Lin, Z.; Paz, F.A.A.; Rocha, J.; Huang, W.; Carlos, L.D. Visible-Light Excited Luminescent Thermometer Based on Single Lanthanide Organic Frameworks. *Adv. Funct. Mater.* **2016**, *26*, 8677–8684. [CrossRef]
11. Cui, Y.; Song, R.; Yu, J.; Liu, M.; Wang, Z.; Wu, C.; Yang, Y.; Wang, Z.; Chen, B.; Qian, G. Dual-Emitting MOF⊃ ⋂ Dye Composite for Ratiometric Temperature Sensing. *Adv. Mater.* **2015**, *27*, 1420–1425. [CrossRef]
12. Wang, Z.; Ananias, D.; Carné-Sánchez, A.; Brites, C.; Imaz, I.; Maspoch, D.; Rocha, J.; Carlos, L. Lanthanide-Organic Framework Nanothermometers Prepared by Spray-Drying. *Adv. Funct. Mater.* **2015**, *25*, 2824–2830. [CrossRef]
13. Ćirić, A.; Ristić, Z.; Antić, Ž.; Dramićanin, M.D. An approximate deconvolution method for the luminescence intensity ratio calculations from overlapping emissions. *Phys. B Condens. Matter* **2022**, *624*, 413454. [CrossRef]
14. Wan, Y.; Cui, Y.; Yang, Y.; Qian, G. Nonlinear optical metal-organic frameworks for ratiometric temperature sensing in physiological range. *Chin. Chem. Lett.* **2021**, *32*, 1511–1514. [CrossRef]
15. Zheng, T.; Runowski, M.; Woźny, P.; Barszcz, B.; Lis, S.; Vega, M.; Llanos, J.; Soler-Carracedo, K.; Martín, I.R. Boltzmann vs. non-Boltzmann (non-linear) thermometry—Yb3+-Er3+ activated dual-mode thermometer and phase transition sensor via second harmonic generation. *J. Alloys Compd.* **2022**, *906*, 164329. [CrossRef]
16. Zheng, T.; Runowski, M.; Martín, I.R.; Lis, S.; Vega, M.; Llanos, J. Nonlinear Optical Thermometry—A Novel Temperature Sensing Strategy via Second Harmonic Generation (SHG) and Upconversion Luminescence in $BaTiO_3$: Ho^{3+},Yb^{3+} Perovskite. *Adv. Opt. Mater.* **2021**, *9*, 2100386. [CrossRef]
17. Ćirić, A.; Periša, J.; Zeković, I.; Antić, Ž.; Dramićanin, M.D. Multilevel-cascade intensity ratio temperature read-out of Dy3+ luminescence thermometers. *J. Lumin.* **2022**, *245*, 118795. [CrossRef]
18. Ćirić, A.; Marciniak, Ł.; Dramićanin, M.D. Luminescence intensity ratio squared—A new luminescence thermometry method for enhanced sensitivity. *J. Appl. Phys.* **2022**, *131*, 114501. [CrossRef]
19. Sheldrick, G.M. *SHELXT*—Integrated space-group and crystal-structure determination. *Acta Crystallogr. Sect. A Found. Adv.* **2015**, *71*, 3–8. [CrossRef]

20. Brito-Santos, G.; Gil-Hernández, B.; Hernández-Rodríguez, C.; González-Díaz, B.; Guerrero-Lemus, R.; Sanchiz, J. [Eu(pta)3me-phen] CCDC Reference Number 2169076 Manuscript in Preparation. 2022. Available online: https://www.ccdc.cam.ac.uk/structures/? (accessed on 10 September 2022).
21. Fomina, I.G.; Dobrokhotova, Z.V.; Kazak, V.O.; Aleksandrov, G.G.; Lysenko, K.A.; Puntus, L.N.; Gerasimova, V.I.; Bogomyakov, A.S.; Novotortsev, V.M.; Eremenko, I.L. Synthesis, Structure, Thermal Stability, and Magnetic and Luminescence Properties of Dinuclear Lanthanide(III) Pivalates with Chelating N-Donor Ligands. *Eur. J. Inorg. Chem.* **2012**, *2012*, 3595–3610. [CrossRef]
22. Sun, Q.; Yan, P.; Niu, W.; Chu, W.; Yao, X.; An, G.; Li, G. NIR luminescence of a series of benzoyltrifluoroacetone erbium complexes. *RSC Adv.* **2015**, *5*, 65856–65861. [CrossRef]
23. Bünzli, J.-C.G.; Piguet, C. Taking advantage of luminescent lanthanide ions. *Chem. Soc. Rev.* **2005**, *34*, 1048–1077. [CrossRef]
24. Martín-Ramos, P.; Coya, C.; Lavín, V.; Martín, I.R.; Ramos Silva, M.; Pereira Silva, P.S.; García-Vélez, M.; Álvarez, A.L.; Martín-Gil, J. Active layer solution-processed NIR-OLEDs based on ternary erbium(iii) complexes with 1,1,1-trifluoro-2,4-pentanedione and different N,N-donors. *Dalton Trans.* **2014**, *43*, 18087–18096. [CrossRef]
25. Artizzu, F.; Mercuri, M.L.; Serpe, A.; Deplano, P. NIR-emissive erbium–quinolinolate complexes. *Coord. Chem. Rev.* **2011**, *255*, 2514–2529. [CrossRef]
26. D'Vries, R.F.; Álvarez-García, S.; Snejko, N.; Bausá, L.E.; Gutiérrez-Puebla, E.; de Andrés, A.; Monge, M. Multimetal rare earth MOFs for lighting and thermometry: Tailoring color and optimal temperature range through enhanced disulfobenzoic triplet phosphorescence. *J. Mater. Chem. C* **2013**, *1*, 6316–6324. [CrossRef]
27. Dang, S.; Ma, E.; Sun, Z.-M.; Zhang, H. A layer-structured Eu-MOF as a highly selective fluorescent probe for Fe3+ detection through a cation-exchange approach. *J. Mater. Chem.* **2012**, *22*, 16920–16926. [CrossRef]
28. Shen, X.; Yan, B. A novel fluorescence probe for sensing organic amine vapors from a Eu^{3+} β-diketonate functionalized bio-MOF-1 hybrid system. *J. Mater. Chem. C* **2015**, *3*, 7038–7044. [CrossRef]
29. Brito-Santos, G.; Gil-Hernández, B.; Martín, I.R.; Guerrero-Lemus, R.; Sanchiz, J. Visible and NIR emitting Yb(iii) and Er(iii) complexes sensitized by β-diketonates and phenanthroline derivatives. *RSC Adv.* **2020**, *10*, 27815–27823. [CrossRef]
30. Liu, X.; Akerboom, S.; de Jong, M.; Mutikainen, I.; Tanase, S.; Meijerink, A.; Bouwman, E. Mixed-Lanthanoid Metal–Organic Framework for Ratiometric Cryogenic Temperature Sensing. *Inorg. Chem.* **2015**, *54*, 11323–11329. [CrossRef]
31. Yang, X.; Zou, H.; Sun, X.; Sun, T.; Guo, C.; Fu, Y.; Wu, C.L.; Qiao, X.; Wang, F. One-Step Synthesis of Mixed Lanthanide Metal–Organic Framework Films for Sensitive Temperature Mapping. *Adv. Opt. Mater.* **2019**, *7*, 1900336. [CrossRef]
32. Kovalenko, A.; Rublev, P.O.; Tcelykh, L.O.; Goloveshkin, A.S.; Lepnev, L.S.; Burlov, A.S.; Vashchenko, A.A.; Marciniak, Ł.; Magerramov, A.M.; Shikhaliyev, N.G.; et al. Lanthanide Complexes with 2-(Tosylamino)-benzylidene-*N*-(aryloyl)hydrazones: Universal Luminescent Materials. *Chem. Mater.* **2019**, *31*, 759–773. [CrossRef]
33. Li, S.; Meng, Q.; Lü, S.; Sun, W. Study on optical temperature sensing properties of Tb3+, Eu3+ co-doped CaMoO4 phosphor. *J. Lumin.* **2018**, *200*, 103–110. [CrossRef]
34. Feng, J.-F.; Yan, X.-Y.; Ji, Z.-Y.; Liu, T.-F.; Cao, R. Fabrication of Lanthanide-Functionalized Hydrogen-Bonded Organic Framework Films for Ratiometric Temperature Sensing by Electrophoretic Deposition. *ACS Appl. Mater. Interfaces* **2020**, *12*, 29854–29860. [CrossRef] [PubMed]
35. Wu, L.-L.; Zhao, J.; Wang, H.; Wang, J. A lanthanide(iii) metal–organic framework exhibiting ratiometric luminescent temperature sensing and tunable white light emission. *CrystEngComm* **2016**, *18*, 4268–4271. [CrossRef]
36. Feng, J.-F.; Liu, T.-F.; Shi, J.; Gao, S.-Y.; Cao, R. Dual-Emitting UiO-66(Zr&Eu) Metal–Organic Framework Films for Ratiometric Temperature Sensing. *ACS Appl. Mater. Interfaces* **2018**, *10*, 20854–20861. [CrossRef] [PubMed]
37. Zhou, Y.; Yan, B.; Lei, F. Postsynthetic lanthanide functionalization of nanosized metal–organic frameworks for highly sensitive ratiometric luminescent thermometry. *Chem. Commun.* **2014**, *50*, 15235–15238. [CrossRef]
38. Ding, M.; Hou, J.; Cui, Z.; Gao, H.; Lu, C.; Xi, J.; Ji, Z.; Chen, D. Bundle-shaped β-NaYF4 microrods: Hydrothermal synthesis, Gd-mediated downconversion luminescence and ratiometric temperature sensing. *Ceram. Int.* **2018**, *44*, 7930–7938. [CrossRef]
39. Kaczmarek, A.M. Eu^{3+}/Tb^{3+} and Dy^{3+} POM@MOFs and 2D coordination polymers based on pyridine-2,6-dicarboxylic acid for ratiometric optical temperature sensing. *J. Mater. Chem. C* **2018**, *6*, 5916–5925. [CrossRef]
40. Jin, C.; Zhang, J. Upconversion luminescence of Ca2Gd8(SiO4)6O2:Yb3+-Tm3+-Tb3+/Eu3+ phosphors for optical temperature sensing. *Opt. Laser Technol.* **2019**, *115*, 487–492. [CrossRef]
41. Li, L.; Tang, X.; Wu, Z.; Zheng, Y.; Jiang, S.; Tang, X.; Xiang, G.; Zhou, X. Simultaneously tuning emission color and realizing optical thermometry via efficient Tb3+→Eu3+ energy transfer in whitlockite-type phosphate multifunctional phosphors. *J. Alloys Compd.* **2019**, *780*, 266–275. [CrossRef]
42. Miyata, K.; Konno, Y.; Nakanishi, T.; Kobayashi, A.; Kato, M.; Fushimi, K.; Hasegawa, Y. Chameleon Luminophore for Sensing Temperatures: Control of Metal-to-Metal and Energy Back Transfer in Lanthanide Coordination Polymers. *Angew. Chem. Int. Ed.* **2013**, *52*, 6413–6416. [CrossRef]
43. Han, L.; Liu, J.; Liu, P.; Li, B.; Li, X.; Xu, Y. Dual-emissive Eu3+, Tb3+ co-doped Gd2(MoO4)3 phosphor for optical thermometry application. *J. Phys. Chem. Solids* **2021**, *153*, 110032. [CrossRef]
44. Ding, M.; Zhang, H.; Chen, D.; Xi, Q.H.J.; Ji, Z. Color-tunable luminescence, energy transfer and temperature sensing behavior of hexagonal NaYF4:Ce3+/Tb3+/Eu3+ microcrystals. *J. Alloys Compd.* **2016**, *672*, 117–124. [CrossRef]
45. Hu, F.; Zhao, Z.; Chi, F.; Wei, X.; Yin, M. Structural characterization and temperature-dependent luminescence of CaF2 :Tb3+ /Eu3+ glass ceramics. *J. Rare Earths* **2017**, *35*, 536–541. [CrossRef]

46. Xi, J.; Ding, M.; Zhang, M.; Zhang, H.; Chen, D.; Ji, Z. Monodispersed YF3:Ce3+/Tb3+/Eu3+ mesocrystals: Hydrothermal synthesis and optical temperature sensing behavior. *J. Mater. Sci. Mater. Electron.* **2017**, *28*, 9489–9494. [CrossRef]
47. Yao, L.-Q.; Zeng, Z.-J.; Chen, G.-H.; Zhong, H.-J.; Cui, S.-C.; Wen, C. Tunable luminescence and temperature sensing behavior of Tb3+/Eu3+ co-doped borate glasses. *J. Mater. Sci. Mater. Electron.* **2016**, *27*, 8402–8407. [CrossRef]
48. Cadiau, A.; Brites, C.D.S.; Costa, P.M.F.J.; Ferreira, R.A.S.; Rocha, J.; Carlos, L.D. Ratiometric Nanothermometer Based on an Emissive Ln^{3+}-Organic Framework. *ACS Nano* **2013**, *7*, 7213–7218. [CrossRef]
49. Alves, L.L.S.; de Lima, R.C.; Schiavon, M.A.; Gonçalves, R.R.; Barbosa, H.P.; Ferrari, J.L. Photoluminescence properties of the material based on SiO2–Y2O3:Eu3+,Tb3+ under different in situ temperature prepared by the sol-gel process. *J. Lumin.* **2020**, *222*, 117109. [CrossRef]
50. Guo, N.; Pan, Y.; Lv, W.; Ouyang, R.; Shao, B. Optical thermometric properties in Tb3+ and Eu3+-coactivated dual-emissive fluorophosphate phosphors. *Opt. Laser Technol.* **2020**, *123*, 105938. [CrossRef]
51. Chen, D.; Wang, Z.; Zhou, Y.; Huang, P.; Ji, Z. Tb3+/Eu3+: YF3 nanophase embedded glass ceramics: Structural characterization, tunable luminescence and temperature sensing behavior. *J. Alloys Compd.* **2015**, *646*, 339–344. [CrossRef]
52. Han, Y.-H.; Tian, C.-B.; Li, Q.-H.; Du, S.-W. Highly chemical and thermally stable luminescent Eu_xTb_{1-x}MOF materials for broad-range pH and temperature sensors. *J. Mater. Chem. C* **2014**, *2*, 8065–8070. [CrossRef]
53. Brites, C.; Millán, A.; Carlos, L. Lanthanides in Luminescent Thermometry. In *Handbook on the Physics and Chemistry of Rare Earths*; Elsevier: Amsterdam, The Netherlands, 2016; pp. 339–427. [CrossRef]
54. Vennettilli, M.; Saha, S.; Roy, U.; Mugler, A. Precision of Protein Thermometry. *Phys. Rev. Lett.* **2021**, *127*, 098102. [CrossRef]